Insights into the effect of structural heterogeneity in carbonized electrospun fibrous mats for flow battery electrodes by X-ray tomography

*Matt Kok, Rhodri Jervis, Dan Brett, Paul Shearing, and Jeff Gostick**

M. D. R. Kok

845 Sherbrook St West, Montreal, H3A 0G4, Canada

Dr. R. Jervis, Prof. D. Brett, Prof. P. R. Shearing

Roberts Building, Torrington Place, London, WC1E 7JE, UK

Prof. J. T. Gostick

259 Philip St, Waterloo, N2L 3W8, Canada

jgostick@uwaterloo.ca

Keyword: X-ray computed tomography; electrospun electrode; flow battery; Lattice Boltzmann Method; porous media

Abstract

Electrospun custom made flow battery electrodes were imaged in 3D using X-ray computed tomography. A variety of computational methods and simulations were applied to the images to determine properties including the porosity, fiber size and pore size distributions as well as the material permeability and flow distributions. The simulations were performed on materials before and after carbonization to determine the effect it had in the internal microstructure and material properties. It was found that the deposited fiber size was constantly changing throughout the electrospinning process. The results also showed that the surfaces of the fibrous material were the most severely altered during carbonization and that the rest of the material remained intact. Pressure driven flow was modelled using the Lattice Boltzmann Method and excellent agreement with experimental results was found. The simulations coupled with the material analysis also demonstrated the highly heterogeneous nature of the flow. Most of the flow would be concentrated to regions with high porosity while regions with low porosity would shield other pores and starve them of flow. The importance of imaging these materials in 3D is highlighted throughout.

1 Introduction

Porous media, and specifically fibrous media, are essential to a wide variety of technologies ranging from traditional filtration membranes, to biomedical applications and advanced electrochemical systems. Electrospinning, a method of preparing fibrous media by which nano and micro fibers are ‘spun’ from a solution using a large voltage potential (> 10 kV), has become

a common means of producing fibrous materials with customized structures. The main appeal of electrospinning, aside from the simplicity of the equipment required, is the tunability of the method [1], allowing the generation of fibers from as small as tens of nanometers to several microns with a wide array of morphologies. In biomedical applications, recent work has utilized electrospun polycaprolactone/gelatin composite materials for guided bone regeneration [2], drug delivery in soft tissue [3,4] and wound dressings based on biodegradable polymers such as polyetherimide [5], polylactic acid [6], and others [7–9]. In electrochemistry, electrospun materials are being employed in a range of devices, such as lithium-ion battery separators [10–13]. These mats can also be carbonized [14] to produce electrically conductive materials for use as Li-ion battery anodes [15,16], and gas diffusion layers in polymer electrolyte membrane fuel cells [17]. Recently, carbonized electrospun mats were used as flow-through electrodes in flow batteries [18,19]. Flow batteries offer a potential solution to grid-scale energy storage due to their reliability, relatively cheap and simple components, and the decoupling of power (determined by the size of the cell) and energy (determined by the volume of electrolyte storage) which makes them flexible to the needs of many different systems [20].

Transport in porous materials, and therefore the performance of devices which employ porous components, is strongly coupled to their micro-structural properties. Features such as the pore size, porosity, tortuosity, connectivity, and even pore shape, have significant impact on the behavior of the material. To understand this complex relationship between pore microstructure, and device performance, there is a strong drive to visualize porous materials in 3D [21], which has been met by the recent advances in X-ray computed tomography (CT). For engineered porous materials such as flow battery electrodes, the ability to see the internal microstructure provides

essential feedback into the quality and consistency of the manufacturing process. Beyond visual inspection, the images can be subjected to a variety of image analysis techniques for quantifying structural properties that correlate with performance. Ultimately, numerical simulations of flow and other transport processes can be conducted directly on the images, called direct numerical simulation (DNS), to predict the material's performance based on the image.

In this work, X-ray CT is used to visualize a variety of electrospun fibrous materials that were produced for use as flow-battery electrodes [19]. The advantage of electrospun materials for this application is the small fiber diameter (usually < 1 μm) which leads to higher specific surface area. However, this creates a significant challenge for their characterization and the ability to model systems employing them, since even the routine step of quantifying fiber sizes requires analysis using two-dimensional imaging techniques (scanning electron microscopy, SEM) that by their nature only describe the outer surface of the sample. Other key properties, such as porosity, are also challenging to assess because the samples themselves are quite thin (~200 μm). Although the porosity of an electrospun material can be measured in the macroscopic sense [22], it is not possible to analyze the distribution of porosity throughout the material. X-ray CT has been employed with great success in the characterization of electrochemical systems such as batteries [23–27], supercapacitors [28], solid oxide fuel cells [29–35] and polymer electrolyte membrane (PEM) fuel cells [36–39]. Recently, CT has also been applied to commercially available flow battery electrode materials [40–42]. This work presents the first X-ray computed tomographic images of electrospun polyacrylonitrile before and after carbonization into electrodes, with resolutions between 360 and 400 nm per voxel, allowing properties such as porosity and fiber diameter to be accurately determined throughout the whole sample. Tomography in conjunction with high-

performance computing has allowed the first complete analysis of the internal structures and morphology of an electrospun material. Using structural images from X-ray CT with computational fluid dynamic modelling we have studied the complex flow through electrospun materials and obtained information on velocity and pressure distributions, areas of stagnation and other flow issues present in inhomogeneous materials. The present work demonstrates the ability of X-ray CT to capture sufficient microstructural detail over a sufficient large field-of-view to obtain meaningful information about the impact of the complex structure on flow behavior, and represents a significant step in the understanding and modelling of the transport process taking place in a flow battery electrode and the further optimization of their manufacture.

2 Methodology

2.1 Material Production

The electrospun materials were generated in-house on a custom made system. The spin dope was pumped by a syringe pump, through a tube connected to a grounded needle. Throughout the duration of the electrospinning the needle was rastered on a linear motion actuator slowly at a speed of 5 mms^{-1} and a 4-inch rotating drum collector was used. Together these precautions ensured consistent material properties across a relatively large sample. The power was supplied by a negative polarity power supply (Glassman, MJ20N0400-11) which was connected to the drum to create the high voltage difference necessary for electrospinning [43]. The spin dope was pumped at a rate of 0.5-0.8 $mLhr^{-1}$ through a 16 gauge stainless steel needle placed 15 cm from the collector which was rotating at 0.5 ms^{-1}. The collector was held at a potential of -15 kV.

The spin dope consisted of polyacrylonitrile (PAN) (Sigma, MW 150,000) dissolved at 12-13 wt% in anhydrous N,N-dimethylformamide (Sigma, 99.8%). This range of concentrations was specifically chosen to generate materials to be used as flow battery electrodes, as such it was desired to make larger fibers than are typically achieved with electrospinning. It has been shown that the optimal fiber diameter for a porous flow battery electrode should be in the 1-2 μm range [18] which is 3-5× larger than the usual range for electrospun PAN [1]. For electrospun materials, the largest parameter affecting the size of the fibers is the concentration of polymer in the spin dope. 12-13 wt% was chosen because this is the maximum concentration of PAN in DMF that can effectively be pumped and electrospun; at higher concentrations, the electrospinning process becomes very unstable.

Some of the produced materials were carbonized in an inert environment furnace to create electrically conductive materials suitable for flow battery electrodes [19]. The material was first stabilized in air, with a heating rate of 5°Cmin^{-1} and a plateau at 250°C for 75 min. Argon was introduced at 25 cm^3min^{-1} after the sample has been stabilized for an hour. The temperature was continually increased at a rate of 5°Cmin^{-1}, plateauing at 850°C and 1050°C both for 40 min. During the carbonization process, the materials are held under slight compression between two ceramic plates. More details about the material production steps can be found elsewhere [19].

2.2 Tomography

Imaging of the electrospun materials was conducted using a Zeiss Xradia Versa 520 micro-CT instrument (Carl Zeiss XRM, Pleasanton, CA), operating with a source voltage of either 30 or 40 kV. The instrument, which utilizes a two stage magnification system, coupling geometrical

magnification with an optically coupled scintillator is described elsewhere [44]. It was found that a low source voltage and a sample diameter of 1 mm or less was required to obtain a good quality image due to the highly porous and low-Z nature of the materials. 1601-2201 projections of 30 s exposure each were recorded through an angular sample rotation of 360°. Reconstruction of the X-ray transmission images was conducted using a filtered back-projection reconstruction algorithm (XM Reconstructor, Zeiss). Use of a 20× objective lens and binning of 1 yielded a voxel size of 0.36 – 0.40 µm in the reconstructed 3D data. The grey-scale reconstructed volume was then segmented into a binary image using Avizo Fire software (Thermo Fisher Scientific, Waltham, MA, USA) to designate pixels as either 'fiber' or 'pore' materials by thresholding based on their grey-scale value. These binarised data sets are then exported as image stacks and used as the structures for the computer modelling.

2.3 Lattice Boltzmann Method

Pressure-driven viscous flow was simulated in-plane using the Lattice Boltzmann Method (LBM) [45]. This numerical model was implemented in the open-source LB solver Palabos [46], using a 3D D3Q19 single relaxation time model with the standard Bhatnagar-Gross-Krook (BGK) collision operator. The initial conditions held the velocity at zero everywhere and fluid movement was induced by applying a fixed pressure gradient between the inlet and the outlet [47]. All other boundaries had a zero flux no-slip boundary condition applied. Convergence was determined by the standard deviation of the average energy of the system reaching 10^{-6}. To ensure Stokes flow ($Re<<1$) the simulation was performed with pressure gradients ranging over several orders of magnitude and results outside this range were discarded. For true Stokes flow, the material permeability of the system will not change with pressure. Further confirmation was achieved by

determining the Reynolds number for the velocity distribution; in all cases, the $Re < 10^{-2}$ was achieved.

2.4 Material Structural Properties

All computational analysis was performed in Python on the binarised volumetric images obtained from the processing of the X-ray CT data. Extracting structural features from tomography images, such as fiber diameter, porosity, pore size distributions, and so on, is the first level of information that one typically obtains. A number of commercial and open-sources packages are available for this (i.e. GeoDict, Avizo, Dragonfly), but it is still often necessary to devise custom methods for specific materials.

2.4.1 Fiber Diameter

Several schemes were considered for estimating fiber diameter distributions, both in the statistical sense and the spatial sense. The first method was to obtain a skeleton of the fiber phase, also known as a medial axis, meaning it lies at the center of the phase and is maximally distance from the fiber surfaces. This skeleton image was then used as a mask on the distance transform (**Figure 1** right) of the solid phase, and the non-zero values were converted to a histogram to get a statistical fiber size distribution [48]. It was also possible to look at the locations of non-zero voxels and plot statistical distributions for given locations, such as different though-plane positions. One downfall of using the skeleton as a mask is that it assigns equal weights to all fiber sizes when creating the histograms, while clearly larger diameter fibers constitute a larger proportion of the solid volume. To address this possible bias, a second approach known as the local thickness was used, where each voxel in the solid phase is assigned the radius of the

largest sphere that can be drawn in the solid phase and overlapping that voxel [49]. (This is not to be confused with the distance transform which finds the largest sphere that can be *centered* on a given voxel, the histogram of which is called the *pore size density* function by Torquato and co-workers [50]). To obtain the local thickness, binary image opening is performed with successively larger spherical structuring elements. The solid phase voxels that survive each step are assigned the radius of the structuring element, so that voxels which belong to larger features are assigned larger radius values. A histogram of the local thickness values provides volume weighted distributions, where a small number of large diameter fibers might represent a notable fraction of the distribution. Figure 2 (left) shows an example of the result of the local thickness algorithm.

A final third alternative, which attempts to count the length-weighted average fiber size was also developed. This approach blends the above two approaches, namely it masks the local thickness values with the skeleton of the fiber phase. The result is a list of values that represent the radius of the feature to which they belong but whose frequency is proportional to the length of the feature, not the volume. An example of the 'skeletonized' radius is presented in Figure 2 (right). For the current data, both methods generated very similar results and there was no evidence of skewing. This was likely because while there may be a significant distribution in fiber sizes, there was a low probability of finding a fiber with a diameter several times larger than average, or large enough to alter the distribution. Because determining the 'skeleton' is computationally intensive and essentially an extra step, the volume average method is presented in these results.

2.4.2 Pore Size Estimations

The pore sizes in the samples were also of interest, so several measurements were made. The local thickness method described previously was used on the pore space to give the pore size

distribution (PSD). A version of this method simulating a mercury intrusion porosimeter (MIP-PSD), was also implemented [48]. The major difference between the PSD and the MIP-PSD is the presence of shielding. In MIP, an interior pore can be shielded by a smaller pore closer to the exterior of the sample. The presence of shielding is indicative of heterogeneities in the material, as changes in the local pore size can make regions less accessible. This effect is illustrated in Figure 3. The strength of this effect for a material is called the constrictivity and can be determined by comparing the PSD with the MIP-PSD [51] according to:

$$\beta = \left(\frac{r_{MIN}}{r_{MAX}}\right)^2 \quad (1)$$

where β is the constrictivity, r_{MIN} is the minimum pore radius, defined as the pore radius with 50% passing for the MIP-PSD, and r_{MAX} is the maximum pore radius, defined as the pore radius with 50% passing for the PSD. $\beta \ll 1$ indicates a high degree of constrictivity, or a high bottlenecking effect, whereas a constrictivity close to 1.0 indicates a material with low bottlenecking.

2.4.3 Porosity

As the scans were of cylindrical pillars, the data presented here is of the largest cropped rectangular region that can be placed inside that pillar. The pillar includes the 'top' and 'bottom' of the sample (allowing for some small amount of cropping for the double-sided tape used to secure the sample). The overall sample porosity is obtained by calculating the fraction of the voxels assigned to the pore space to the total voxels in the sample. In this work, the spatial distribution or profiles of porosity was also of interest, particularly the porosity profile in the Z-direction. This is obtained by summing all the void voxels in a given XY plane. Although the

porosity of a plane is technically an area fraction, in the case of voxels each plane represents a 360 nm thick subsection.

2.5 Permeability

The LBM simulation's output was a velocity field (x, y and z components), from which the Darcy permeability could be determined in both lattice and real units. To convert the velocities from lattice to real units we take advantage of the non-dimensionality of the Reynolds number; which should be equal in both domains:

$$Re = \frac{\vec{u}_L L_L}{\nu_L} = \frac{\vec{u} L}{\nu} \tag{2}$$

where $\vec{u}$ is the velocity vector, ν is the kinematic viscosity, the subscript L denotes the lattice domain and no subscript indicates the physical domain. Rearranging gives:

$$\vec{u} = \frac{\nu}{\nu_L}\left(\frac{L_L}{L}\right) u_L \tag{3}$$

where $\left(\frac{L_L}{L}\right)$ is the reciprocal of the lattice distance and ν is the kinematic viscosity of the fluid, taken to be 1.004 m^2s^{-1} or equivalent to water at 20°C and ν_L was taken as 0.16667 (as recommended by the developers of Palabos [46]). The lattice permeability can also be found, which is a perfect analogue to Darcy's law in real units:

$$\vec{q} = -\frac{\kappa}{\mu}\vec{\nabla}P \tag{4}$$

where, $\vec{q}$ is the flux of fluid through the material [$m^3m^{-2}s^{-1}$], μ is the dynamic viscosity of the fluid [$kg{\cdot}m^{-1}s^{-1}$], and $\vec{\nabla}P$ is the pressure gradient [$Pa{\cdot}m^{-1}$]. The flux is determined by taking the average velocity in the direction of flow throughout the material. Every voxel has side lengths of 1 lattice

unit, so in this case the average velocity is equal to the average flux without the need for normalizing. The pressure gradient and the viscosity are provided by the user before operation and are therefore known. It should be noted that technically the user specifies ν, the kinematic viscosity, and the conversion is made assuming the density is unity.

3 Results and Discussion

The data presented here analyses 3D tomography images of four samples, representing PAN concentrations of 12 and 13 wt% in the spin dope, before and after carbonization of the materials. Virtual orthoslices of the 3D volumes generated from the X-ray CT of 12 and 13 wt% carbonized materials are shown in Figure 4 and Figure 5 respectively. The greyscale images from these scans (and those of the uncarbonized materials, not shown) are segmented using the Avizo software suite whereby the voxels are assigned values of zero for the pore phase and one for the fiber phase, based on their greyscale value. 3D representation of these binary data sets are shown in Figure 6, and it is these data sets that are used in the modelling presented here. Figure 7 shows a sample representation of the domains modelled and analyzed throughout the results and discussion. The orientation of the axes will be consistent throughout the analysis. An axis-averaged value (presented in the analysis below) represents the average of a value moving along that axis. Analyzing the results with this spatial variable was found to be essential to understanding behavior of these materials. Fibers are continually added on top of the existing fibers to form a mat that grows as the process progresses. Variations in properties along the thickness (z) direction are caused by electrospinning conditions changing through time. The other two directions (x and y) can be grouped together as ‘in-plane’ (IP). Distribution of properties in

these directions have only to do with the randomness of the electrospinning process and the movement of the rotating drum collector or the rastering of the needle by the linear motion actuator. Both the drum and the needle were moving at very low speeds, so no anisotropy was created and these two directions should show no distribution in properties. For modelling purposes, the in-plane direction (x) is parallel to the direction of flow in the medium; this corresponds to the direction perpendicular to the channels in a redox flow battery, and is visualized as streamlines in Figure 7. The y-direction corresponds to the direction parallel to the channels in a flow battery.

3.1 Fiber Diameter

A key challenge presented by analyzing any porous media is the inability to analyze properties in the core of the material. This is especially true for feature sizes, such as fiber or pore diameter. For micro and nanofibers, effective imaging can only be done using scanning electron microscopy (SEM) which is naturally limited to visualizing only the outer surface of the material. [52] Nonetheless, 2D images of the surface are still widely used to infer structural information about the bulk material. The potential problems with this approach are exacerbated in electrospinning, since the 'top' and the 'bottom' are by no means representative of the interior due to possibly changing spinning conditions through the production. This problem is further aggravated by carbonization, as the fibers at the surfaces are in contact with plates that may cause temperature gradients as well as subjecting the fibers to different forces than experienced throughout the bulk. Obtaining 3D structural information via X-ray CT, as presented in this work, allows these heterogeneities to be discovered and accounted for, and indeed for their effect on the

performance of the electrode to be studied; this is not possible with 2D imaging methods commonly applied to such materials.

Figure 8 (left) shows the fiber diameter distribution in a 12 wt% electrospun material before carbonization, obtained through X-ray CT, and therefore representing the whole material. It should be noted that the sample volume was not perfectly cubic, and therefore the full lengths of the different dimensions are not equal. The electrospinning yielded relatively consistent fiber diameters in all dimensions. There is slightly more variation in the fiber diameter in the through-plane direction as opposed to the in-plane direction; however, it is relatively minor. Figure 8 (left) suggests that estimating the fiber diameter from just the surface information would be a relatively good estimation of the global fiber diameter in this case. This is not always true, however, as can be seen for the same material after carbonization in Figure 8 (right). It can be seen that after carbonization, the fiber diameter in-plane remains relatively constant, but the variation through the thickness of the material (through-plane) is far from constant. At the extremes of this dimension, the 'top' and 'bottom' of the samples, significant deviation from the average values are present. The fibers at the surfaces show a significant decrease in diameter when compared to the rest of the material. A likely explanation for this is the different conditions experienced at the surfaces compared to the bulk of the sample during the carbonization step. At the boundary, the material is in contact with the ceramic plates, which could have created a temperature gradient through the material.

Although having smaller fibers towards the edges and larger fibers in the middle of a sample may not be a significant concern for a given application, from a characterization perspective this is a crucial difference. Analyzing this material after carbonization with SEM would result in an

underestimation of the fiber diameter throughout the material by 25%, leading to highly erroneous estimations of key material properties such as solid surface area and permeability.

The 13 wt% materials (Figure 5) do not show the same type of edge effects present in the 12 wt% materials; however, they further illustrate that insufficient information is obtained by only analyzing the outer surfaces of the materials. Figure 9 shows the fiber diameter distribution for the 13 wt% materials, with the electrospun materials shown on the left and the carbonized materials shown on the right. In this case, the fiber diameter is continually decreasing in the through-plane due to uncontrolled variations in the spinning conditions. It is unclear why carbonization doesn't have the same effect in both samples. A possible explanation could be that the 13 wt% material was significantly more compressed during carbonization (as seen in Figure 10 (bottom)) which potentially decrease the heterogeneities in the compression profile.

In general, Figure 8 and Figure 9 also demonstrate that the carbonizing process does not necessarily lead to the reduction in fiber diameter that is expected. In both the 12 and 13 wt% cases, the carbonized material follows the overall scale as well as the shape of the electrospun material rather closely, excluding some edge effects.

3.2 Porosity

Figure 10 shows the porosity distribution in all dimensions for all samples. The 12 and 13 wt% materials are shown on the top and bottom, respectively, while the left side shows the electrospun materials before carbonization and the right side after carbonization. There are two main features to be shown in these distributions. Firstly, as was the case with the fiber diameters, much of the variability is in the through-plane direction, representing time throughout the

electrospinning process. The smooth distributions in-plane indicate the rotating drum collector and linear motion actuator were effective in ensuring an even distribution of fibers during the electrospinning process. Much like with the fiber diameters discussed in the previous section, the 12 wt% material doesn't exhibit a trend in either direction; there is some variability but it remains relatively constant throughout. On the other hand, the 13 wt% material has a general increasing trend in porosity that matches the decreasing fiber diameters shown in Figure 9. Assuming the rotating drum collector and the linear motion rastering perform ideally, a decreasing fiber diameter should lead to an increase in porosity, so the trend seen in the porosity of the 13 wt% materials is expected.

The second observation that can be made from Figure 10 is that materials lose porosity during the carbonization process. [19] There are two possible explanations; firstly, the compression applied by the ceramic plates during the carbonization process reduces the pore space and therefore reduces the porosity. Secondly, as materials are carbonized they lose mass. [19] If the fibers are remaining relatively constant in diameter, it's possible they are losing mass evenly throughout, causing them to contract and reducing the pore space between fibers.

3.3 Pore Size Distributions

The pore size distributions determined using the simulated MIP experiment as well as the local thickness are shown in Figure 11. Unsurprisingly, in every case the local thickness method showed larger values than the MIP simulation. The constrictivity value for every material was calculated using these curves and the results are tabulated in Table 1. The constrictivities of the materials do not vary significantly, with the exception that the 12 wt% uncarbonized material is higher. This

material has the most consistent fiber size (Figure 8) and the highest and most consistent porosity (Figure 10). These consistent properties lead to a material that is not prone to bottle necking and overly constricted flow.

An example 3D rendering of the 12 wt% carbonized material can be seen in Figure 12.The left of the image shows the local size determined by a MIP simulation while the right shows the local pore sizes determined by the local thickness method. The pore sizes have been thresholded to the same value for each image to relieve clutter. This allows for the direct comparison of the two images. Anything on the right that doesn't appear on the left is being affected by shielding and bottlenecking.

3.4 Permeability

The LBM simulations allowed for the determination of the fluid velocity distribution on the pore level but also the determination of the Darcy permeability on the material level. Permeability is a key parameter for most porous media modelling studies, as it determines the material's resistance to flow and is often used as a 'continuum' property to fully describe the material's interactions with fluid flow. To validate the velocity distributions achieved through the LBM simulations, the material permeability determined from the simulations was compared to experimental data [19] on the same materials in Figure 13. The experimental results match the results determined through LBM quite closely. The reason for the relatively close data clustering of LBM results is that the materials were imaged under no compression and only one sample was imaged. The experimental data was measured under a series of compressions, leading to a variety of different porosity values and a wider distribution.

Examining the spatial velocity distributions in the materials provides further insights into the effects of fiber size and material porosity on permeability. The permeability distributions through the material were determined using the method described above, but on one plane at a time. In essence, the magnitude of velocity across a plane is averaged over the pore space in that plane. This value is treated as the flux for the purpose of calculating permeability by Darcy's law. When analyzed in this way the permeability distribution is more a 'contribution to permeability' distribution as permeability is by definition a continuum value without distributions, especially on a pore scale. Plotting this distribution versus the fiber diameter and porosity in the through-plane direction is illuminating. Figure 14 shows the permeability distribution compared to both the porosity distribution on the left and fiber diameter distribution on the right, for the 12 wt% carbonized material. The permeability clearly tracks the porosity quite closely, although there does seem to be some confounding effect of the fiber size that is likely an artifact of the highly coupled nature of fiber diameter and pore size in electrospun materials.

To get a more quantitative picture of the flow heterogeneity, the distribution of flow velocity can be analyzed on a voxel-by-voxel basis, as shown in Figure 15 (left) which is a YZ slice of the 3D velocity field. Clearly visible are pockets of high velocity surrounded by regions of low or almost no flow. If this material were used as a flow-through electrode, a significant portion of the reactive surface area would be starved for reactants.

Additional insights into the heterogenous distribution of the flow can be gained by analyzing the distance transform of the material. Figure 15 (right) shows the distance transform in the pore space for the same slice as shown on the left. There is a correlation between the distance transform and the velocity; all regions of high flow are through large pores; however, the

opposite is not true There are large pores throughout the material that have very low, or even stagnant flow. There are two major contributing causes: the first, known as channeling, is where regions are starved of flow because all the flow has concentrated in one area, due to large pores forming a continuous flow domain. This is very evident in the bottom half of Figure 15 (left), where there are five dominant 'pipes' where most of the flow is concentrated. The second factor, closely related to the first, is shielding where smaller pores prevent flow from reaching the larger pores. To illustrate these points, consider Figure 16 which shows the two planes perpendicular to that shown in Figure 15, intersecting the coordinates y = 60 µm and z = 135 µm, the location with the highest flow.

Figure 16 (top) shows the XZ plane's velocity profile (left) and distance transform (right) clearly illustrates the channeling effect. The flow rate in one small section is five times higher than throughout the rest of the plane. The flow stays on this straight path until it is forced out of plane by a large 'blob' feature, which it travels around. (see Figure 16 bottom right). The XY plane through this region is represented in Figure 16 (bottom). The velocity (left) and distance transform (right) in this case show evidence of shielding. Despite having very similar pores sizes in three regions on the far right of the distance transform. The two regions with smaller pores 'upstream' of them are shielded and have low flows.

To get a more complete picture of the flow velocity distribution, the value of the distance transform versus the fluid velocity was analyzed across the entire 3D image and is plotted in Figure 17 (left). To simplify the results only the centers of the pores were considered. Centers were found using the recently reported SNOW algorithm [53]. Despite the significant scatter, the result is a linear relationship, which was unexpected given that flow through a porous material is

often approximated as flow through a set of cylindrical pipes where velocity scales with the squared-distance from the solid walls. This indicates that in this very high porosity fibrous media, that there is very limited interaction and drag between the fluid and solid. Rotating this plot and plotting the 'z' position on the third axis shows that the highest and lowest velocities are a grouped at different 'z' positions, resulting from varying manufacturing conditions (Figure 17 (right)). This plot essentially quantifies the strong channel effect that can be seen in Figure 16 top, left. The location-specific analysis afforded by this tomography dataset are extremely useful in detecting the presence of heterogeneous structures and their impact on flow conditions. It remains an ongoing task to quantify the impact of these heterogeneities on the actual performance of cells, the prevalence of such uniformities in materials, and more generally the validity of various modeling tools that treat the electrode as a volume-averaged continua or a network of tubes.

4 Conclusions

This paper explores the use of computational methods on 3D tomographic images of electrospun materials, with a specific aim of characterizing the consistency of produced structures. To the best of our knowledge, this is the first time that electrospun fibers have been imaged in 3D at this resolution using this technique. The materials imaged represent 12 and 13 wt% PAN in DMF, both 'as spun' and after carbonization to make electronically conductive materials for electrochemical applications. Custom image analysis tools allowed for the determination of the fiber size and porosity distributions though the materials, as well as simulated mercury intrusion porosimetry experiments and generated pore size distributions. It was found that for both the

fiber diameter and material porosity the only significant variation was in the Z-dimension. Because this dimension corresponds to the electrospinning time, it provides direct evaluation of inconsistent or drifting production conditions. The other two dimensions show a very even distribution, which demonstrates the effectiveness of the rotating drum and the rastering of the electrospinning needle to ensure uniform properties.

The fiber diameter distributions showed two interesting characteristics that are both relevant to the common practice of determining material properties from SEM images. First, because electrospinning is a dynamic process, the fiber size at either surface can give a very poor representation of the fiber size throughout. It was shown that the size of the fibers can possibly change during the entirety of the spinning process. Which side is imaged under SEM can lead to very different ideas about material properties. More generally SEM is limited to two-dimensional images but most properties of interest are linked to percolation and therefore require three-dimensional imaging.

The 12 wt% material showed a very even distribution in fiber size before carbonization, but after carbonization the fiber size on the surfaces was significantly lower. The likely cause for this is compression or temperature gradients during the carbonization process which lead to higher conversion at the edges. This represents a significant issue because had this sample been analyzed with SEM the fiber size, and therefore many material properties, would be incorrect and many assumptions about the carbonization process would be misleading.

The flow distribution in the materials was determined using the Lattice Boltzmann Method. This allowed for the determination of the material permeability which was compared to

experimentally obtained results on the same materials imaged. The LBM permeability showed excellent agreement with the experimental results which validated the flow distributions. Further analysis was done on the distribution of permeability within the materials and it was shown quite clearly that the largest determining factor for permeability was the material porosity. The permeability and flow distributions obtained demonstrate the effect that heterogeneity can have on the performance of these engineered materials. Small variations in fiber diameter and local porosity can double the material permeability, and these changes can happen on a scale of 10's of microns. Imaging these materials with high-resolution X-ray CT provides insights into actual flow that are not available through SEM or continuum modelling alone. The vital importance of using real-life structures, only obtainable through 3D methods such as X-ray CT, to fully understand property distributions in modelling of porous media is highlighted in this study.

5 Acknowledgments

The authors acknowledge support from the EPSRC under grants EP/L014289/1 and EP/N032888/1, as well as the STFC Extended Network in Batteries and Electrochemical Energy Devices (ST/N002385/1) for funding of travel for Rhodri Jervis to Canada. Paul R Shearing acknowledges the support of the Royal Academy of Engineering. This work was supported by the Natural Science and Engineering Research Council (NSERC) of Canada. MDR Kok is grateful to the Eugenie Ulmer Lamothe Endowment as well as the Vadasz Family Doctoral Fellowship for funding his work, as well the McGill University's Graduate Mobility Award for funding his travel to the UK.

6 References

[1] M. D. R. Kok, J. T. Gostick, *J. Membr. Sci.* **2015**, *473*, 237.
[2] K. Ren, Y. Wang, T. Sun, W. Yue, H. Zhang, *Mater. Sci. Eng. C* **2017**, *78*, 324.
[3] A. Nadim, S. N. Khorasani, M. Kharaziha, S. M. Davoodi, *Mater. Sci. Eng. C* **2017**, *78*, 47.
[4] A. Khalf, S. V. Madihally, *Mater. Sci. Eng. C* **2017**, *76*, 161.
[5] T. Haase, A. Krost, T. Sauter, K. Kratz, J. Peter, S. Kamann, F. Jung, A. Lendlein, D. Zohlnhöfer, C. Rüder, *J. Tissue Eng. Regen. Med.* **2017**, *11*, 1034.
[6] A. C. Alavarse, F. W. de Oliveira Silva, J. T. Colque, V. M. da Silva, T. Prieto, E. C. Venancio, J.-J. Bonvent, *Mater. Sci. Eng. C* **2017**, *77*, 271.
[7] M. Zhang, H. Lin, Y. Wang, G. Yang, H. Zhao, D. Sun, *Appl. Surf. Sci.* **2017**, *414*, 52.
[8] G. Perumal, S. Pappuru, D. Chakraborty, A. Maya Nandkumar, D. K. Chand, M. Doble, *Mater. Sci. Eng. C* **2017**, *76*, 1196.
[9] T. Zhou, B. Sui, X. Mo, J. Sun, *Int. J. Nanomedicine* **2017**, *12*, 3495.
[10] X. Ma, P. Kolla, R. Yang, Z. Wang, Y. Zhao, A. L. Smirnova, H. Fong, *Electrochimica Acta* **2017**, *236*, 417.
[11] K. M. Freitag, H. Kirchhain, L. van Wüllen, T. Nilges, *Inorg. Chem.* **2017**, *56*, 2100.
[12] Y. Ding, H. Hou, Y. Zhao, Z. Zhu, H. Fong, *Prog. Polym. Sci.* **2016**, *61*, 67.
[13] M. Yanilmaz, X. Zhang, *Polym. Basel* **2015**, *7*, 629.
[14] L. Zhang, A. Aboagye, A. Kelkar, C. Lai, H. Fong, *J. Mater. Sci.* **2013**, *49*, 463.
[15] Y. Wu, M. V. Reddy, B. V. R. Chowdari, S. Ramakrishna, *ACS Appl. Mater. Interfaces* **2013**, *5*, 12175.
[16] D. Kim, D. Lee, J. Kim, J. Moon, *ACS Appl. Mater. Interfaces* **2012**, *4*, 5408.
[17] S. Chevalier, N. Ge, J. Lee, M. G. George, H. Liu, P. Shrestha, D. Muirhead, N. Lavielle, B. D. Hatton, A. Bazylak, *J. Power Sources* **2017**, *352*, 281.
[18] M. D. R. Kok, A. Khalifa, J. T. Gostick, *J. Electrochem. Soc.* **2016**, *163*, A1408.
[19] S. Liu, M. Kok, Y. Kim, J. L. Barton, F. R. Brushett, J. Gostick, *J. Electrochem. Soc.* **2017**, *164*, A2038.
[20] W. W. W. Wang, *Adv. Funct. Mater.* **2013**, *23*, 970.
[21] B. Tjaden, D. J. L. Brett, P. R. Shearing, *Int. Mater. Rev.* **2016**, *0*, 1.
[22] R. R. Rashapov, J. Unno, J. T. Gostick, *J. Electrochem. Soc.* **2015**, *162*, F603.
[23] Y. K. Chen-Wiegart, P. Shearing, Q. Yuan, A. Tkachuk, J. Wang, *Electrochem. Commun.* **2012**, *21*, 58.
[24] S. J. Cooper, D. S. Eastwood, J. Gelb, G. Damblanc, D. J. L. Brett, R. S. Bradley, P. J. Withers, P. D. Lee, A. J. Marquis, N. P. Brandon, P. R. Shearing, *J. Power Sources* **2014**, *247*, 1033.
[25] M. Di Michiel, J. M. Merino, D. Fernandez-Carreiras, T. Buslaps, V. Honkimäki, P. Falus, T. Martins, O. Svensson, *Rev. Sci. Instrum.* **2005**, *76*, 043702.
[26] D. P. Finegan, M. Scheel, J. B. Robinson, B. Tjaden, I. Hunt, T. J. Mason, J. Millichamp, M. D. Michiel, G. J. Offer, G. Hinds, D. J. L. Brett, P. R. Shearing, *Nat. Commun.* **2015**, *6*, 6924.
[27] D. P. Finegan, E. Tudisco, M. Scheel, J. B. Robinson, O. O. Taiwo, D. S. Eastwood, P. D. Lee, M. Di Michiel, B. Bay, S. A. Hall, G. Hinds, D. J. L. Brett, P. R. Shearing, *Adv. Sci.* **2016**, *3*, n/a.
[28] X. Liu, R. Jervis, R. C. Maher, I. J. Villar-Garcia, M. Naylor-Marlow, P. R. Shearing, M. Ouyang, L. Cohen, N. P. Brandon, B. Wu, *Adv. Mater. Technol.* **2016**, *1*, n/a.

[29] G. J. Nelson, W. M. Harris, J. J. Lombardo, J. R. Izzo Jr., W. K. S. Chiu, P. Tanasini, M. Cantoni, J. Van herle, C. Comninellis, J. C. Andrews, Y. Liu, P. Pianetta, Y. S. Chu, *Electrochem. Commun.* **2011**, *13*, 586.
[30] P. R. Shearing, R. S. Bradley, J. Gelb, F. Tariq, P. J. Withers, N. P. Brandon, *Solid State Ion.* **2012**, *216*, 69.
[31] Y. Guan, W. Li, Y. Gong, G. Liu, X. Zhang, J. Chen, J. Gelb, W. Yun, Y. Xiong, Y. Tian, H. Wang, *J. Power Sources* **2011**, *196*, 1915.
[32] P. R. Shearing, R. S. Bradley, J. Gelb, S. N. Lee, A. Atkinson, P. J. Withers, N. P. Brandon, *Electrochem. Solid-State Lett.* **2011**, *14*, B117.
[33] P. R. Shearing, J. Gelb, J. Yi, W.-K. Lee, M. Drakopolous, N. P. Brandon, *Electrochem. Commun.* **2010**, *12*, 1021.
[34] J. R. Izzo, A. S. Joshi, K. N. Grew, W. K. S. Chiu, A. Tkachuk, S. H. Wang, W. Yun, *J. Electrochem. Soc.* **2008**, *155*, B504.
[35] P. R. Shearing, J. Gelb, N. P. Brandon, *J. Eur. Ceram. Soc.* **2010**, *30*, 1809.
[36] C. Hartnig, I. Manke, R. Kuhn, N. Kardjilov, J. Banhart, W. Lehnert, *Appl. Phys. Lett.* **2008**, *92*, 134106.
[37] C. Hartnig, I. Manke, R. Kuhn, S. Kleinau, J. Goebbels, J. Banhart, *J. Power Sources* **2009**, *188*, 468.
[38] Q. Meyer, N. Mansor, F. Iacoviello, P. L. Cullen, R. Jervis, D. Finegan, C. Tan, J. Bailey, P. R. Shearing, D. J. L. Brett, *Electrochimica Acta* **2017**, *242*, 125.
[39] I. Manke, C. Hartnig, M. Grünerbel, W. Lehnert, N. Kardjilov, A. Haibel, A. Hilger, J. Banhart, H. Riesemeier, *Appl. Phys. Lett.* **2007**, *90*, 174105.
[40] R. Jervis, L. D. Brown, T. P. Neville, J. Millichamp, D. P. Finegan, T. M. M. Heenan, D. J. L. Brett, P. R. Shearing, *J. Phys. Appl. Phys.* **2016**, *49*, 434002.
[41] L. D. Brown, T. P. Neville, R. Jervis, T. J. Mason, P. R. Shearing, D. J. L. Brett, *J. Energy Storage* **2016**, *8*, 91.
[42] P. Trogadas, O. O. Taiwo, B. Tjaden, T. P. Neville, S. Yun, J. Parrondo, V. Ramani, M.-O. Coppens, D. J. L. Brett, P. R. Shearing, *Electrochem. Commun.* **2014**, *48*, 155.
[43] R. S. Barhate, C. K. Loong, S. Ramakrishna, *J. Membr. Sci.* **2006**, *283*, 209.
[44] D. S. Eastwood, R. S. Bradley, F. Tariq, S. J. Cooper, O. O. Taiwo, J. Gelb, A. Merkle, D. J. L. Brett, N. P. Brandon, P. J. Withers, P. D. Lee, P. R. Shearing, *Nucl. Instrum. Methods Phys. Res. Sect. B Beam Interact. Mater. At.* **2014**, *324*, 118.
[45] N. Satofuka, T. Nishioka, *Comput. Mech.* **1999**, *23*, 164.
[46] *Palabos*, FlowKit Ltd, **n.d.**
[47] W. Degruyter, A. Burgisser, O. Bachmann, O. Malaspinas, *Geosphere* **2010**, *6*, 470.
[48] *PoreSpy*, PMEAL, Unversity of Waterloo, **n.d.**
[49] M. Y. M. Chiang, F. A. Landis, X. Wang, J. R. Smith, M. T. Cicerone, J. Dunkers, Y. Luo, *Tissue Eng. Part C Methods* **2008**, *15*, 65.
[50] S. Torquato, *Random Heterogeneous Materials: Microstructure and Macroscopic Properties*, Springer Science & Business Media, **2013**.
[51] O. Stenzel, O. Pecho, L. Holzer, M. Neumann, V. Schmidt, *AIChE J.* **2016**, *62*, 1834.
[52] O. O. Taiwo, D. P. Finegan, D. S. Eastwood, J. L. Fife, L. D. Brown, J. A. Darr, P. D. Lee, D. J. l. Brett, P. R. Shearing, *J. Microsc.* **2016**, *263*, 280.
[53] J. T. Gostick, *Phys. Rev. E* **2017**, *96*, 023307.

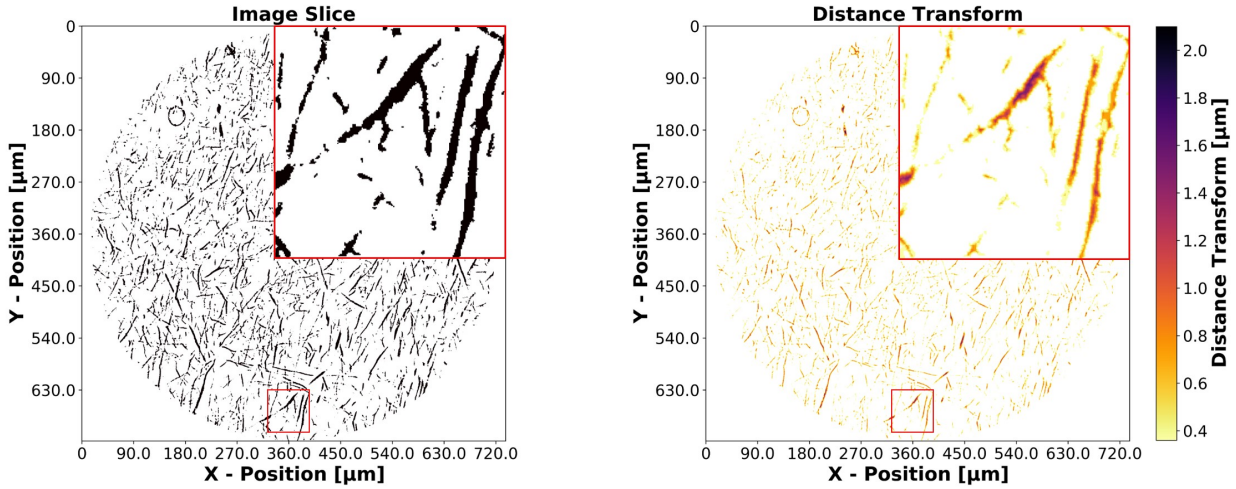

Figure 1: (Left) Image slice showing fibers in white and pore space in black, (Right) Distance Transform in Fiber Space, the numerical values are the distance from each fiber voxel to the nearest pore voxel, approximating the radius of a cylinder

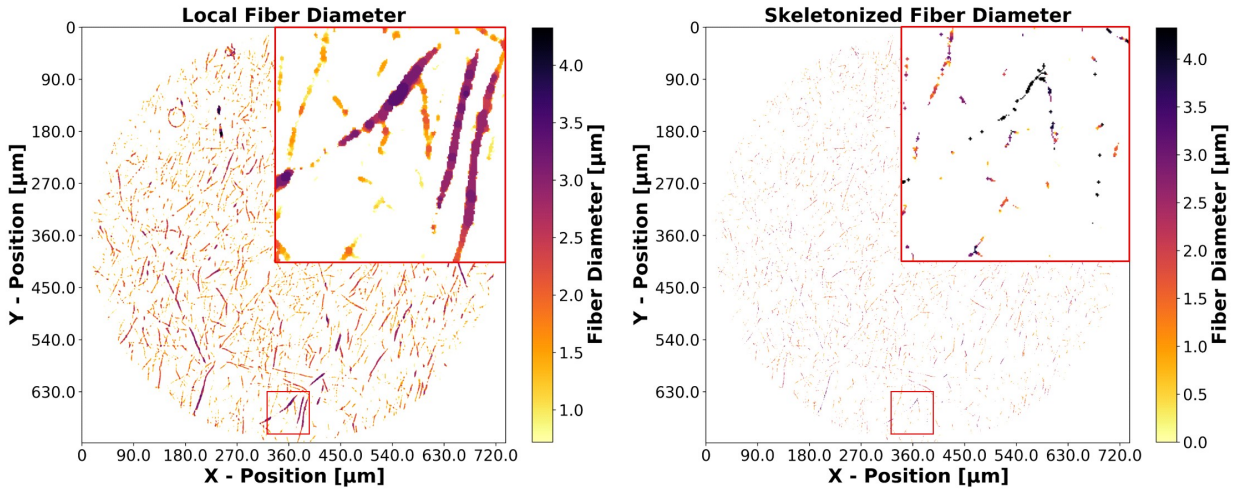

Figure 2: (Left) The local fiber diameter in the form of the local thickness results. These values represent a volume averaged diameter measurement. (Right) The fiber diameter from the local thickness measurement overlaid on the fiber skeleton. These values represent the fiber (length) averaged fiber diameter.

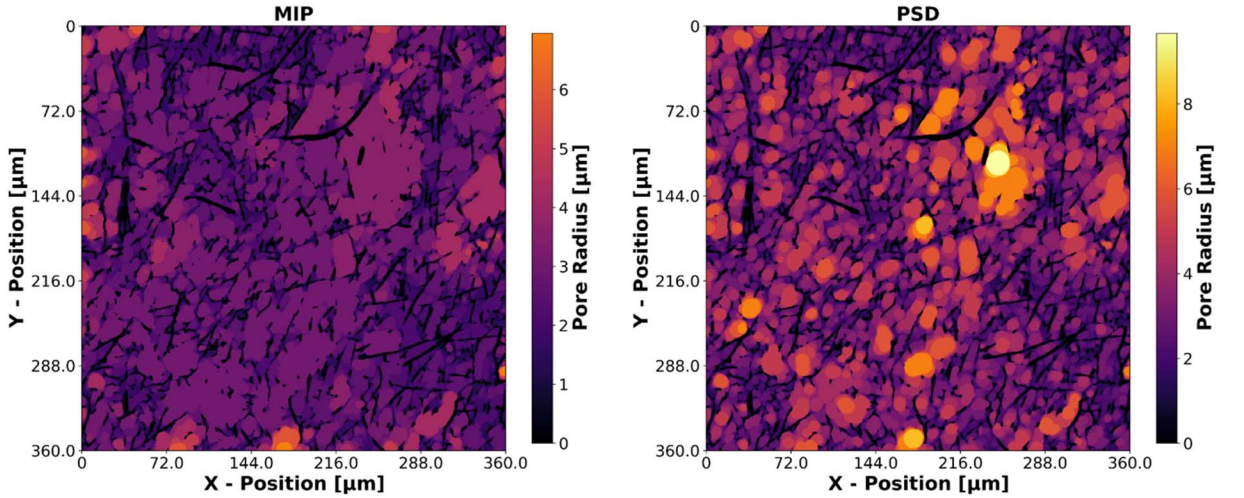

Figure 3: (Left) An orthoslice of a simulated mercury intrusion porosimetry experiment. (Right) An orthoslice of a local thickness measurement used to determine the pores size distribution. The effect of shielding can be very clearly seen as the many large pores in the center of the MIP domain are 'invaded' at smaller radii.

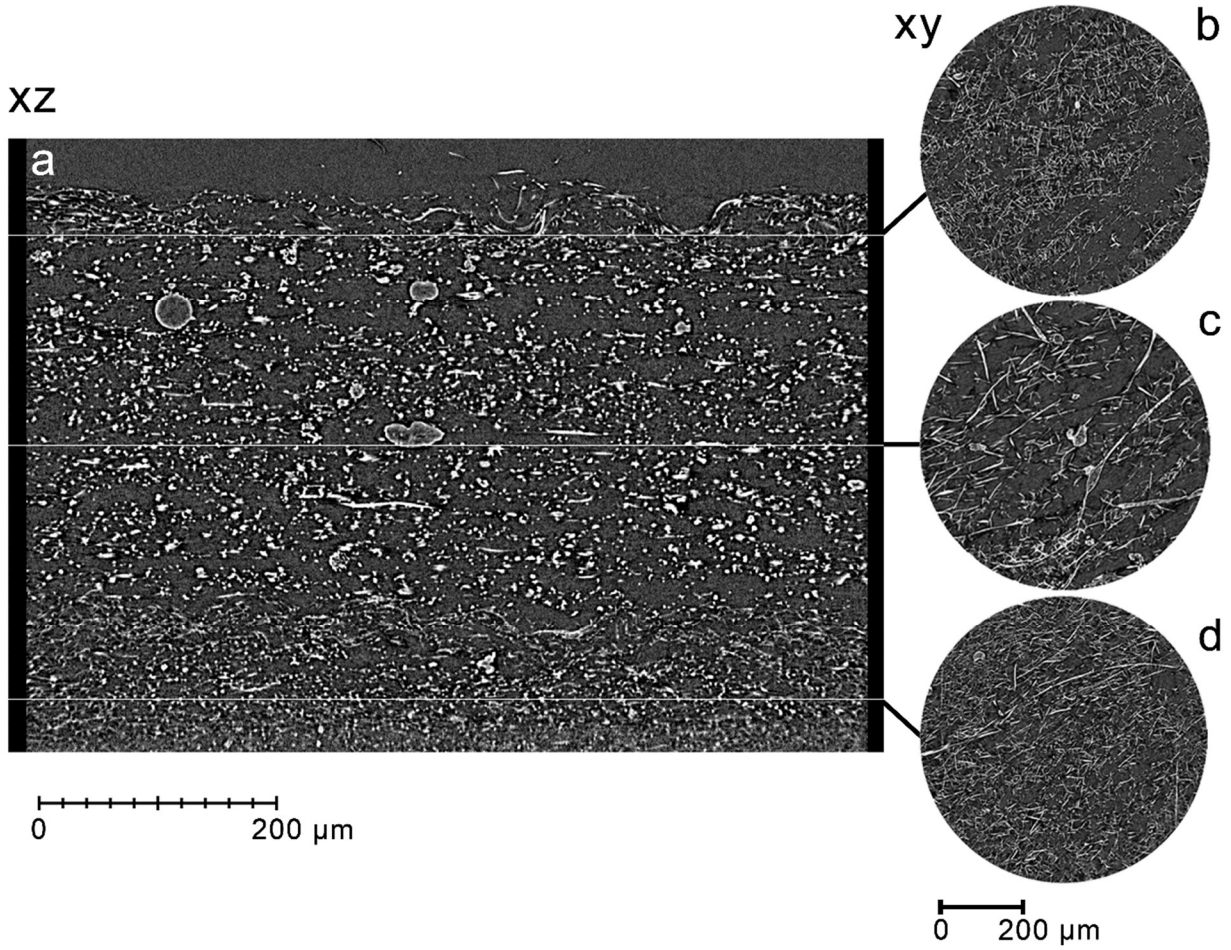

Figure 4: Virtual orthoslices of the reconstructed 3D volume of the 12 wt% carbonized electrospun electrode material, showing the full thickness of the mat through plane (xz, a) and three slices in plane (xy) at different z heights from the top (b), middle (c) and bottom (d) of the sample. A variety of fiber sizes can be seen in the sample with variation throughout the thickness. Image obtained on the Versa 520 XCT machine operating with a source target voltage of 30 kV capturing 2201 projections of 30 s exposure each and resulting in a voxel size of 360 nm

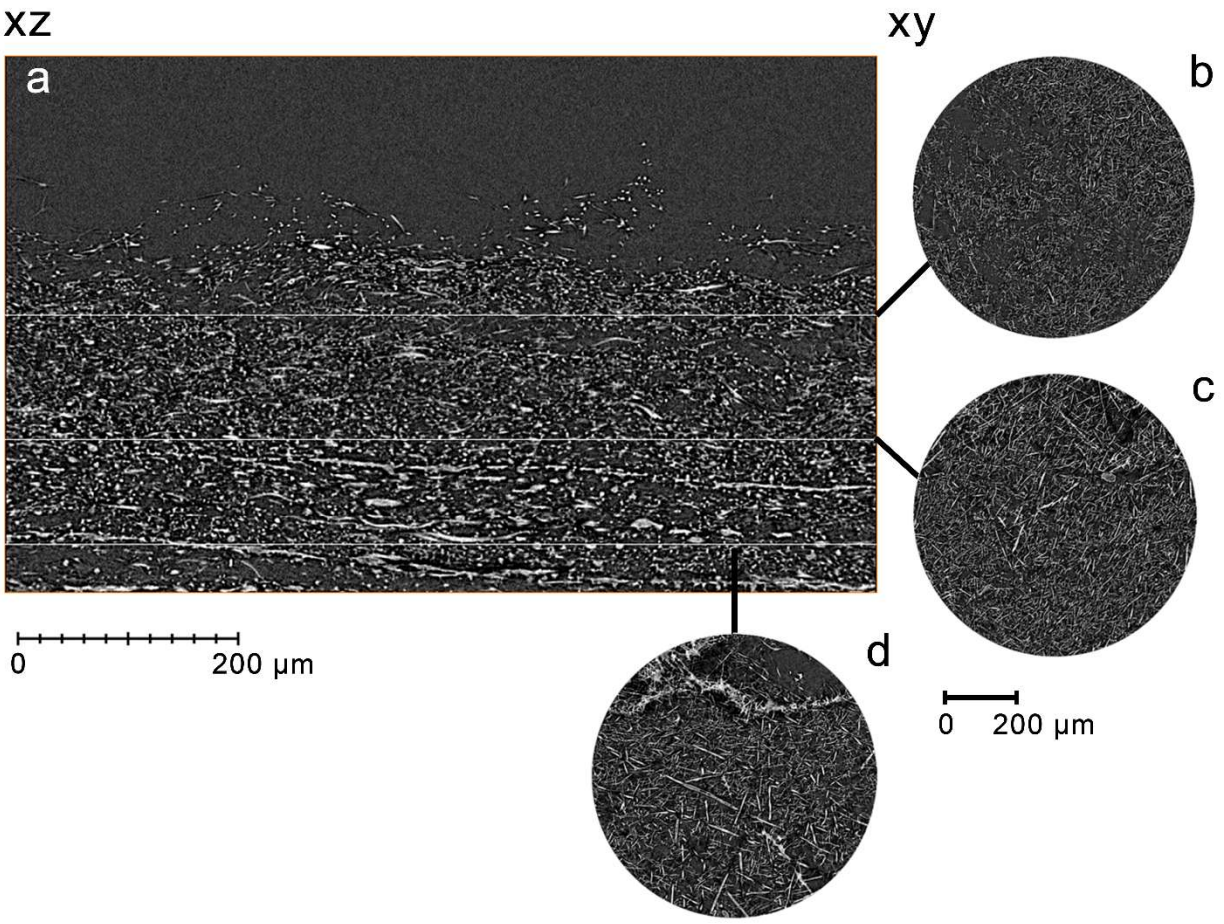

Figure 5: Virtual orthoslices of the reconstructed 3D volume of the 13 wt% carbonized electrospun electrode material, showing the full thickness of the mat through plane (xz, a) and three slices in plane (xy) at different z heights from the top (b), middle (c) and bottom (d) of the sample. Image obtained on the Versa 520 XCT machine operating with a source target voltage of 30 kV capturing 1601 projections of 30 s exposure each and resulting in a voxel size of 400 nm.

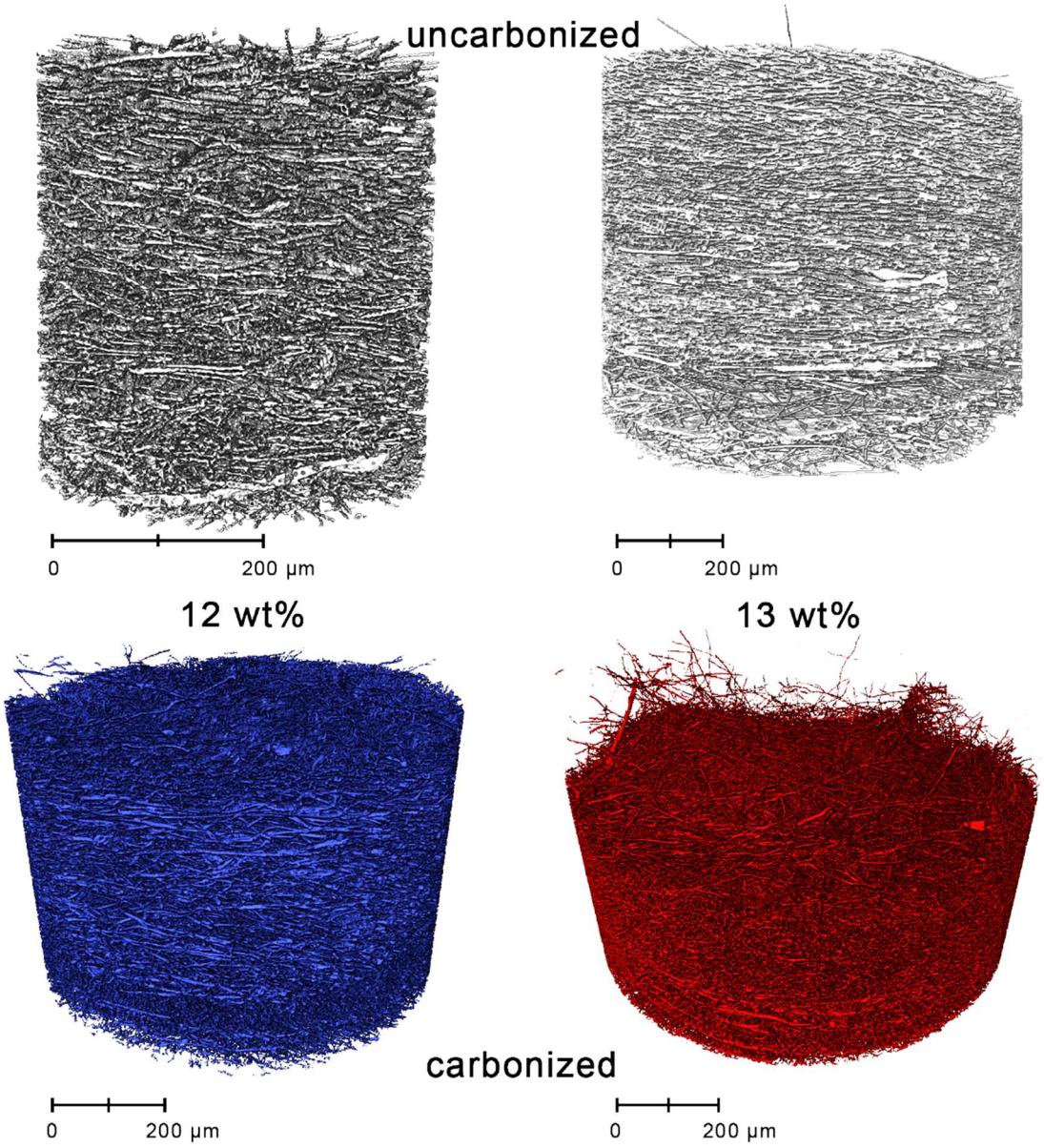

Figure 6: 3D representations of uncarbonized (top, white) and carbonized (bottom, colored) electrospun materials made from a spin dope containing 12 wt % (left) and 13 wt% (right) of PAN. The images shown here are rendered from pixels assigned to the 'fiber' phase using the threshold segmentation tool in the Avizo software suite, and represent the binarized data sets used in the modelling.

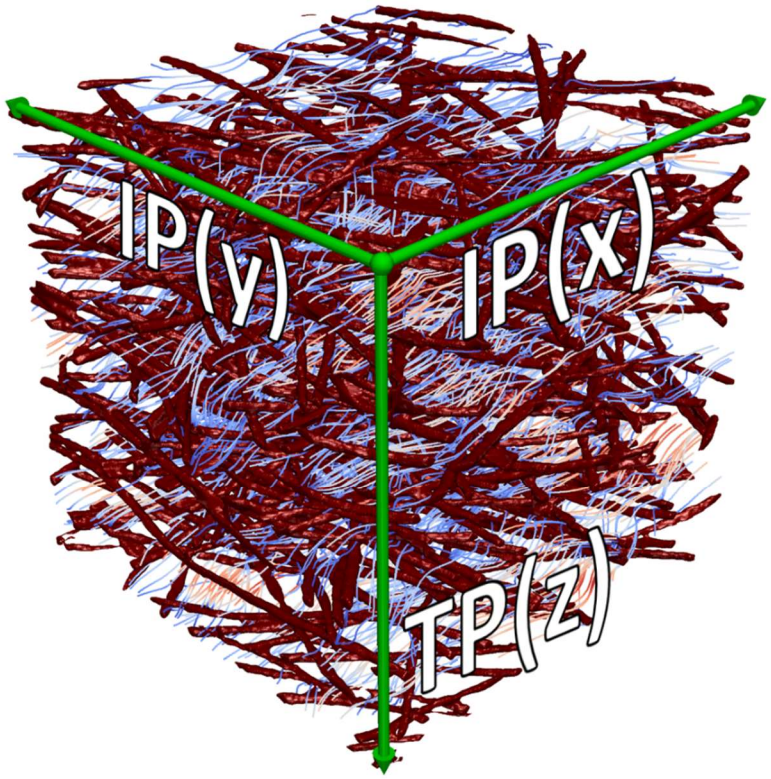

Figure 7: Representation of the modelled domain. Streamlines obtained through LBM show the direction of flow (z-axis). The x-axis represents the electrospinning time while the y-axis is across the domain.

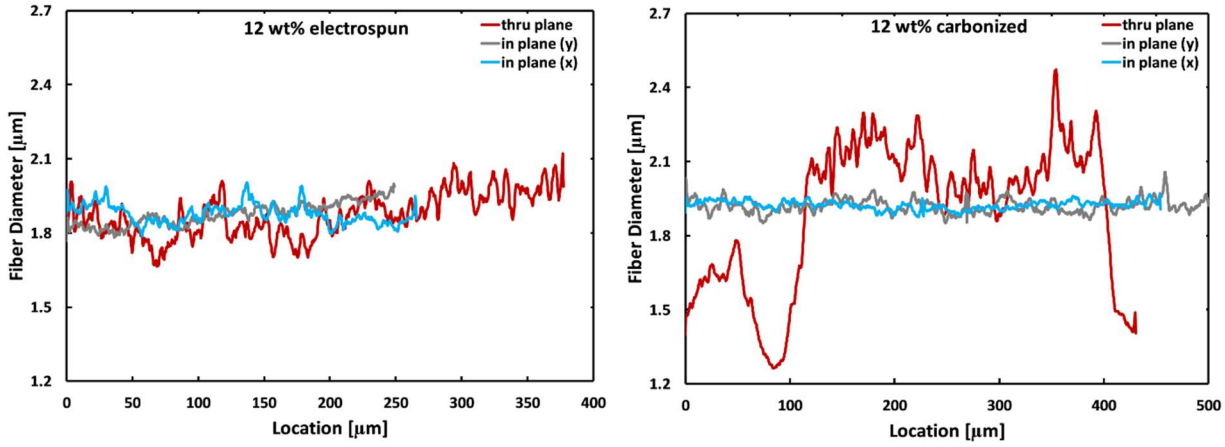

Figure 8: Fiber diameter distribution for all axes in a 12 wt% material. Left shows the distributions before the carbonization process. Right shows after carbonization.

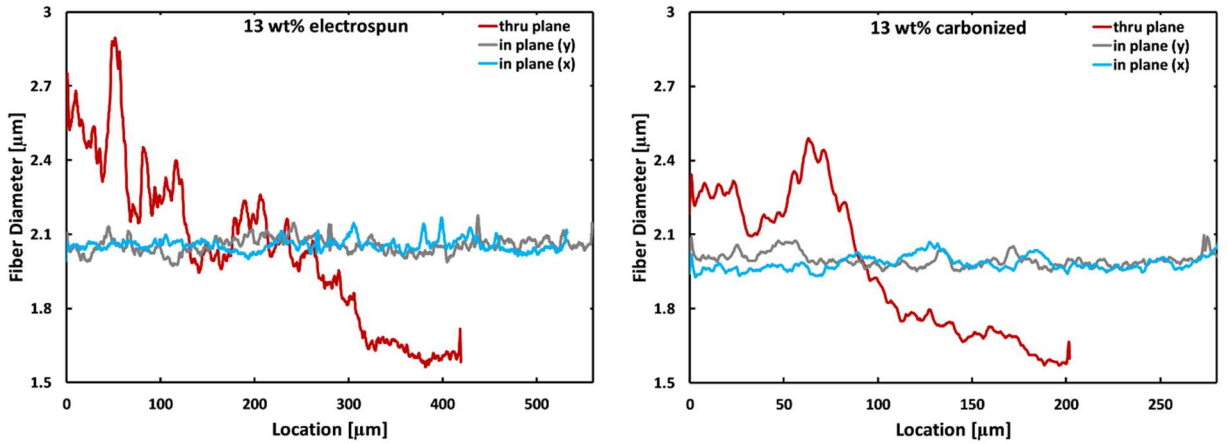

Figure 9: Fiber diameter distribution for all axes in a 13 wt% material. Left shows the distributions before the carbonization process. Right shows after carbonization

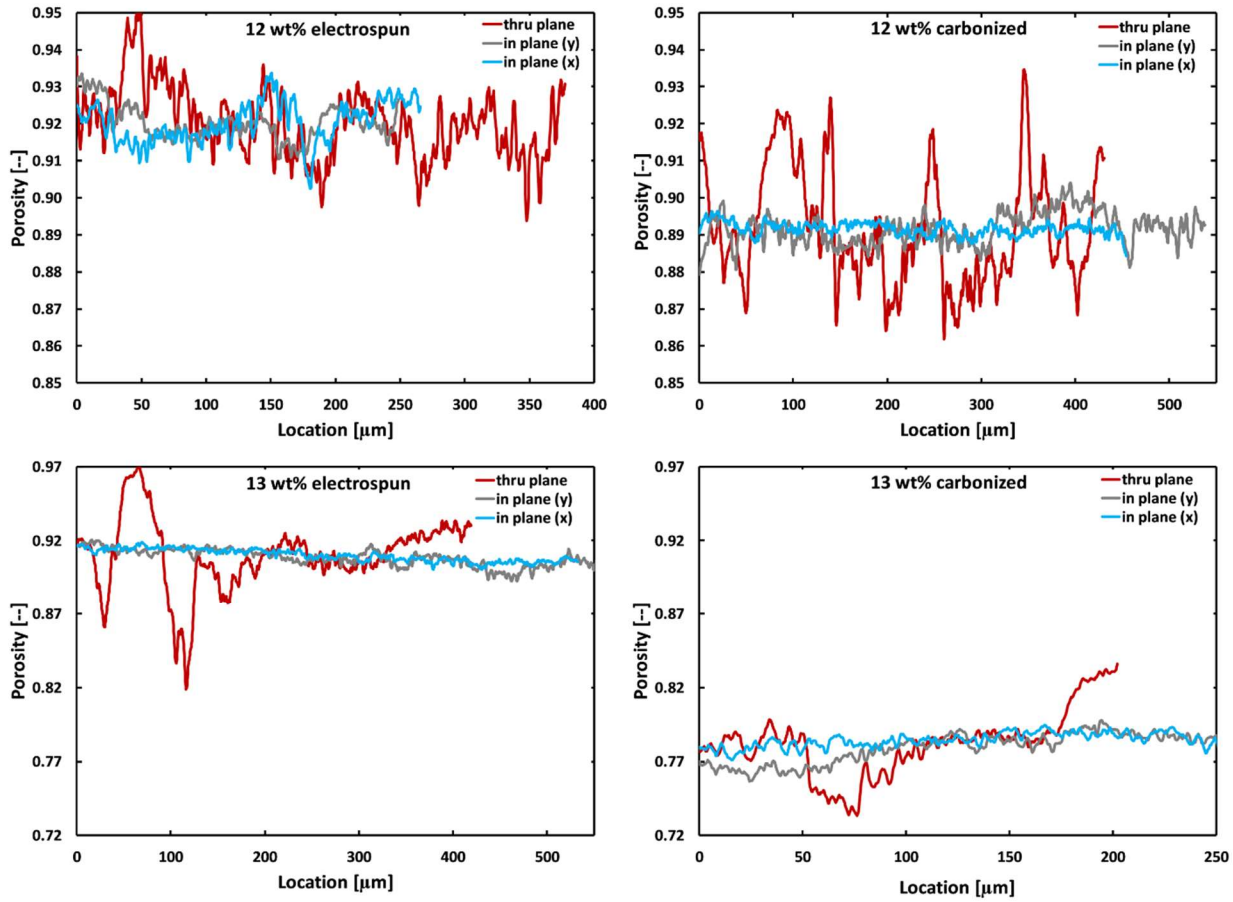

Figure 10: Porosity distribution for all samples. The top row shows 12 wt% data and the bottom row 13 wt% data. The electrospun samples are on the left and the carbonized materials are on the right.

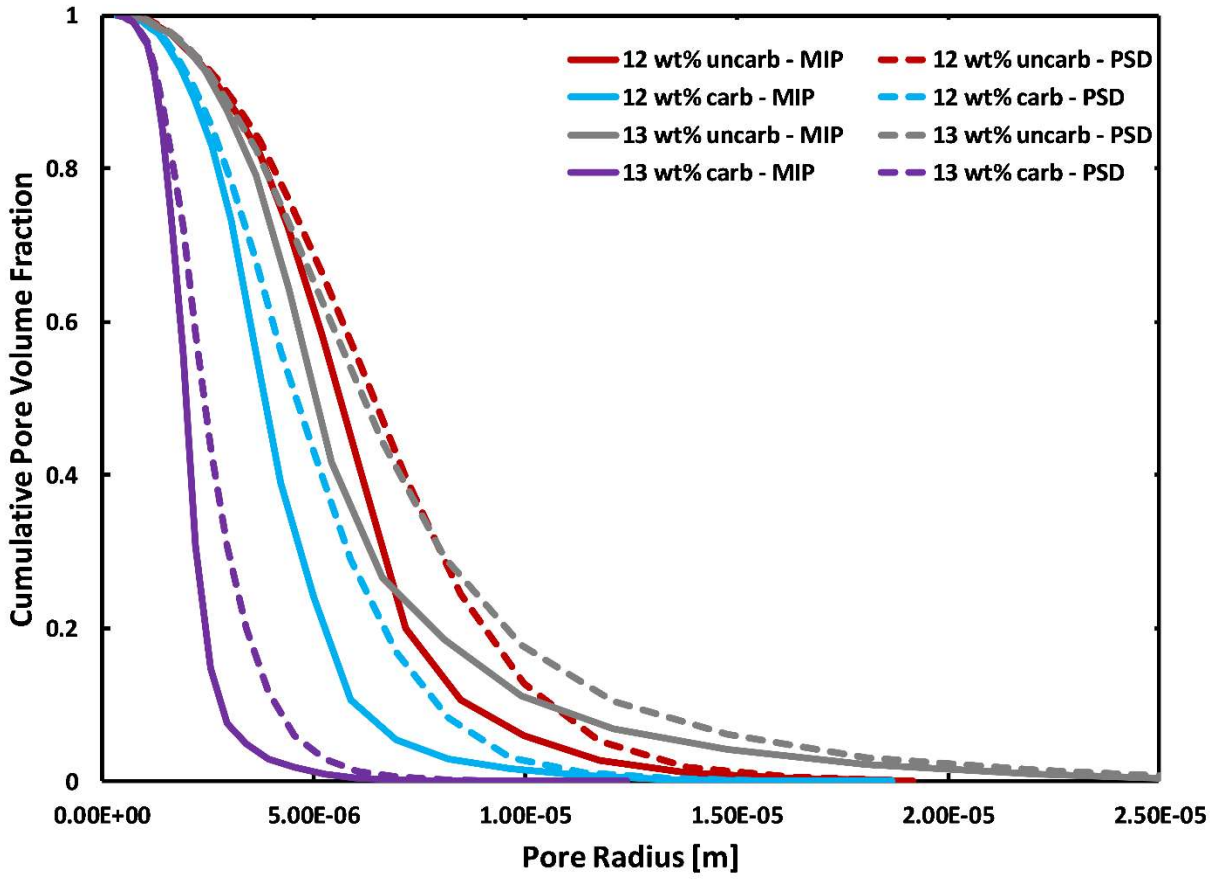

Figure 11: Pore size distributions for all materials. The solid lines indicate an MIP experiment while the hashed lines show the true PSD by way of the local thickness technique

Table 1: Minimum and maximum pore radii and constrictivity values for all samples.

	r_{MIN} [µm]	r_{MAX} [µm]	β [--]
12 wt% uncarbonized	5.64	6.43	0.767
12 wt% carbonized	3.82	4.59	0.692
13 wt% uncarbonized	5.04	6.09	0.685

13 wt% carbonized	2.00	2.41	0.690

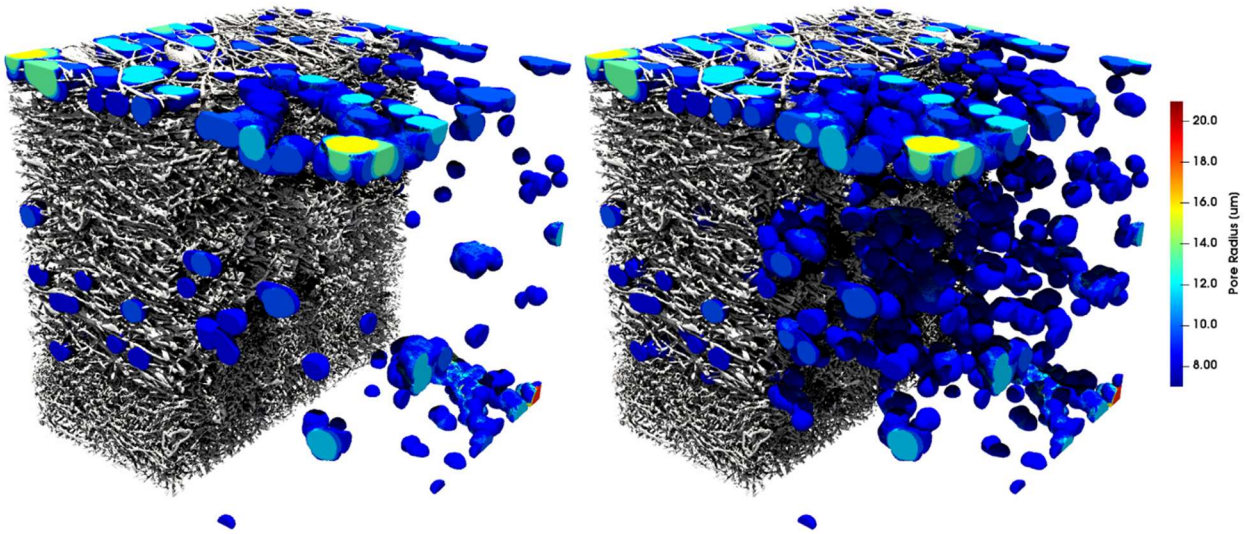

Figure 12: 3D rendering 12 wt% carbonized material. The image on the left shows the local pore sizes determined by an MIP simulation while the right shows the local pore sizes determined by the local thickness method. The pore sizes have been thresholded to the same value in each image to relieve clutter.

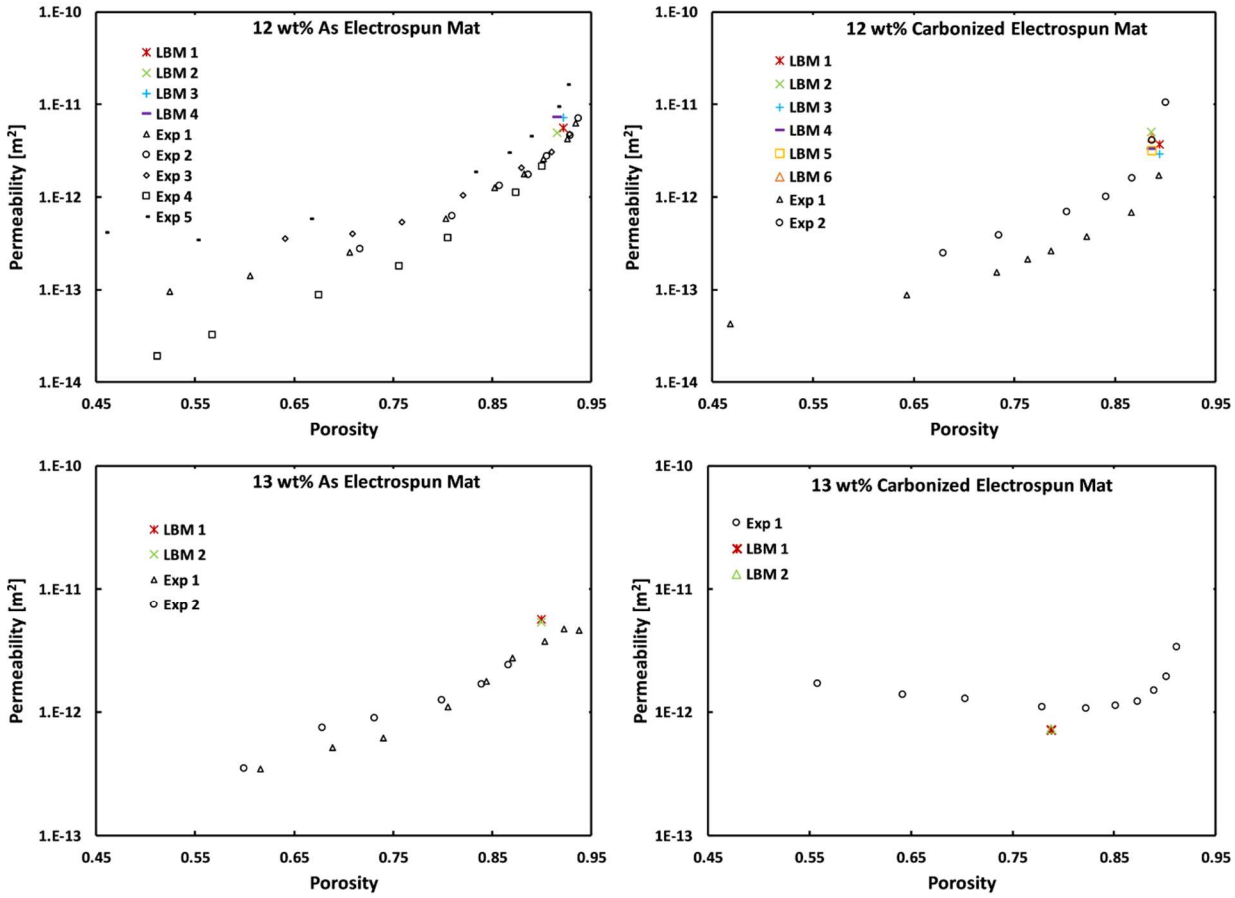

Figure 13: Comparison of Darcy Permeability determined through LBM with experimental data. The top row shows the 12 wt% material and the bottom row shows the 13 wt% material. The electrospun materials are on the left and the carbonized materials are on the right.

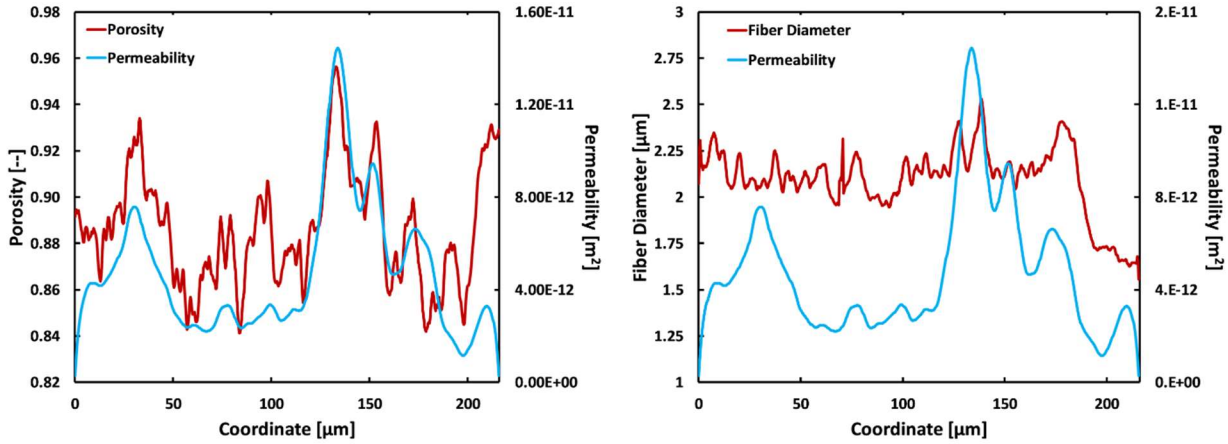

Figure 14: Permeability distribution versus (left) porosity and (right) fiber diameter. Both samples are taken from an in-plane simulation on the 12 wt% carbonized materia.

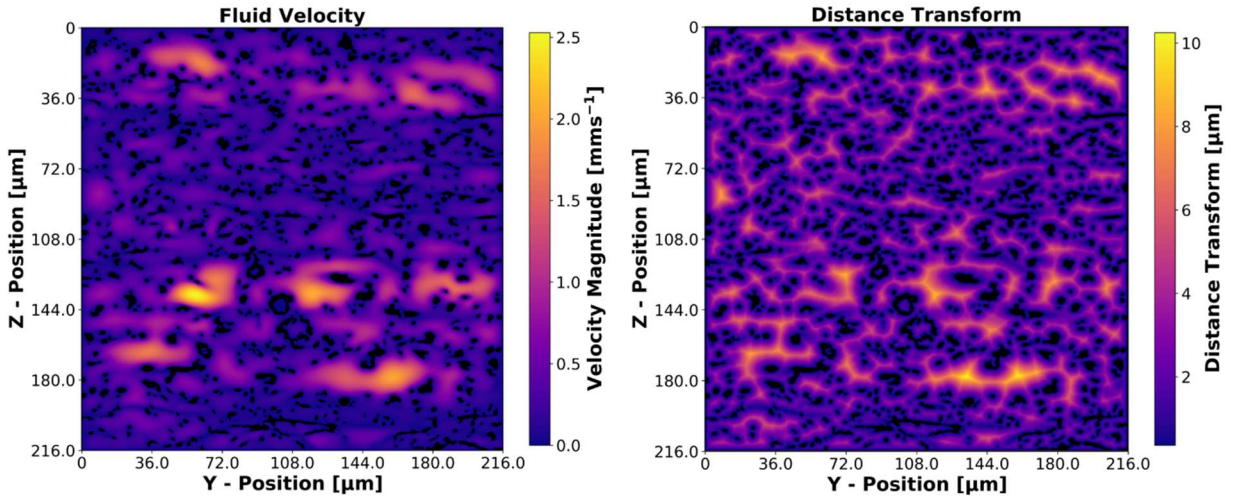

Figure 15: (Left) Fluid velocity through a YZ 'slice' of porous material. The fluid is flowing perpendicular to the plane of the image. Zero flow (black) represents the fiber phase. The material shown here is of the 12 wt% carbonized material. (Right) The distance transform in the pore space for that same plane

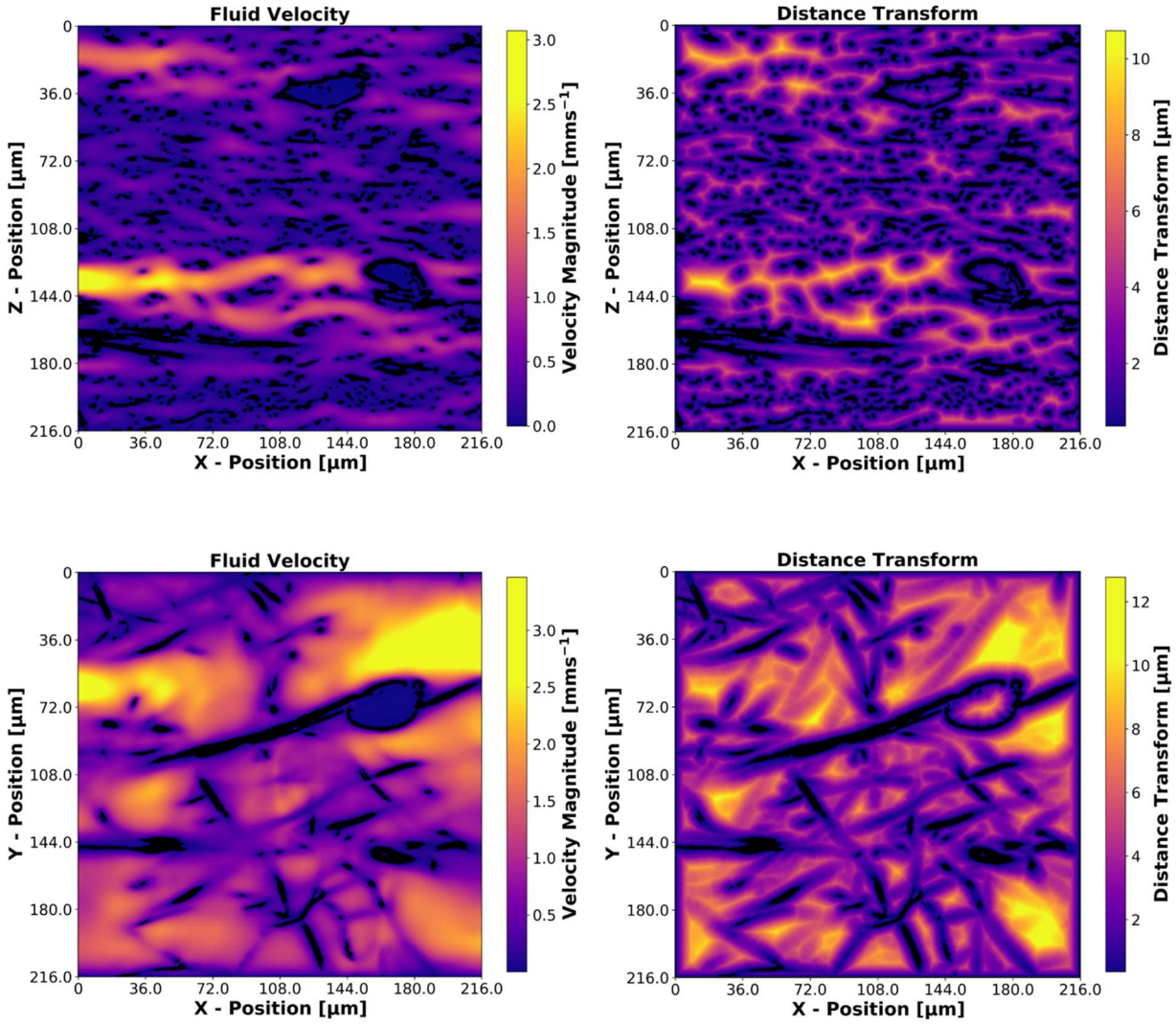

Figure 16: (Top left) The fluid velocity profile for a XZ plane; the material is flowing from left to right in this image. (Top right) The distance transform of that same plane. This 'slice' shows the area for y = 60 µm in Figure 15. (Bottom left) The fluid velocity profile for a XY plane; the material is flowing from left to right in this image. (Bottom right) The distance transform of that same plane. This 'slice' shows the shows the area for z = 135 µm in Figure 15.

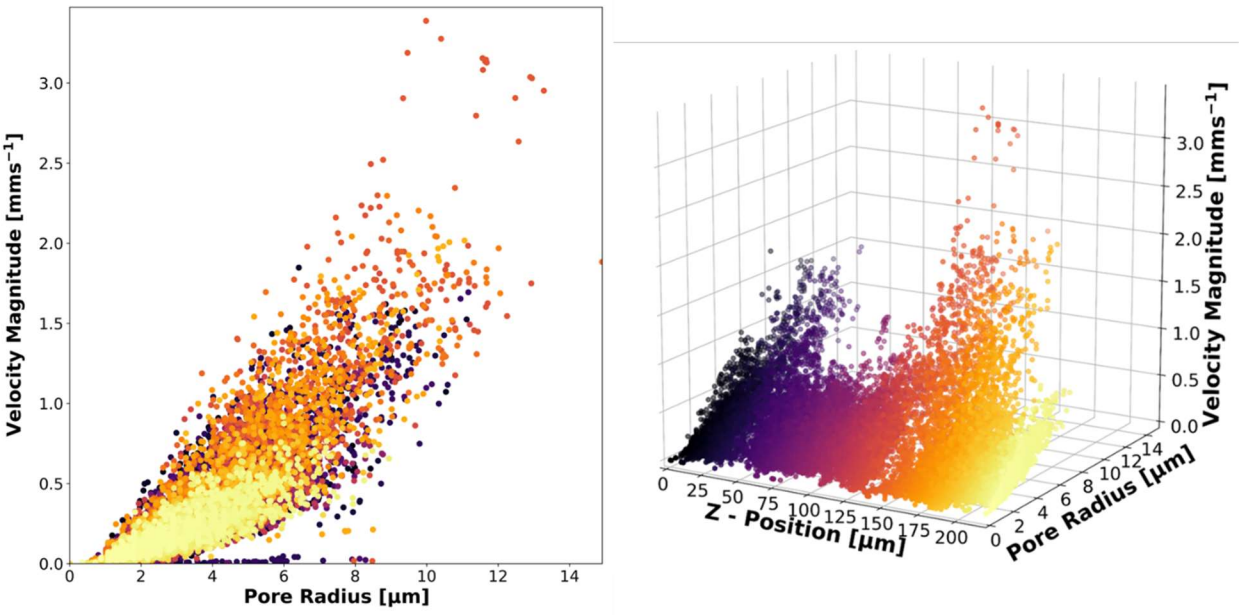

Figure 17: (Left) Velocity magnitude vs pore radius for all pores in domain. The colors help to visualize the different 'z' positions. (Right) A 3D rotated version of the left figure where the 'z' position is expressed along the depth of the figure.

Table of Contents entry:

Exploring the effect of imperfect and non-homogenous fibrous structure in electrospun flow battery electrodes by X-ray computed tomography and direct numerical simulations. Flow is modelled in 3D images of pre and post carbonization electrospun fibrous electrodes. Resulting heterogeneous flow patterns are analyzed with pore size distributions, mercury intrusion porosimetry drainage curves, porosity and fiber size distributions to determine underlying cause.

Keyword: X-ray computed tomography; electrospun electrode; flow battery; Lattice Boltzmann Method; porous media

*Matt Kok, Rhodri Jervis, Dan Brett, Paul Shearing, and Jeff Gostick**

Title: Insights into the effect of structural heterogeneity in carbonized electrospun fibrous mats for flow battery electrodes by X-ray tomography

ToC Figure: